



Dynamic failure of metallic pyramidal truss core materials – Experiments and modeling

S. Lee ^a, F. Barthelat ^a, J.W. Hutchinson ^b, H.D. Espinosa ^{a,*}

^a *Department of Mechanical Engineering, Northwestern University, 2145 Sheridan Road, Evanston, IL 60208, USA*

^b *Division of Engineering and Applied Sciences, Harvard University, Cambridge, MA 02138, USA*

Received 13 August 2005; received in final revised form 2 December 2005

Available online 29 March 2006

Abstract

The quasi-static and dynamic compressive behavior of pyramidal truss cores made of 304 stainless steel were investigated using a combination of experimental techniques. Quasi-static tests were performed using a miniature loading stage while a Kolsky bar apparatus was used to investigate intermediate deformation rates. High deformation rates were examined using a light gas gun. Optical imaging of the sample deformation was performed in real time by means of high-speed photography. In this article, we provide a quantification of load-deformation response and associated failure modes across the sample as captured by high-speed photography. A finite element model is formulated and thorough simulations performed to understand the roles of material strain rate hardening and structural microinertia. Deformation modes were identified from acquired images, force-deformation histories and numerical modeling. Comparison between force-deformation histories under quasi-static and Kolsky bar loading reveals a moderate microinertia effect as manifested by a small increase in peak compressive stress. At high deformation rates, gas gun experiments, a totally different deformation mode is manifested with a major increase in peak compressive stress. In this case, the inertia associated to the bending and buckling of truss struts played a significant role. This effect appears to dominate the early truss core response because of two effects: (i) the propagation of a plastic wave along the truss members; (ii) buckling induced lateral motion. These findings are consistent with prior theoretical and computational work carried out by Vaughn et al. (2005) [Vaughn, D. Canning, M., Hutchinson, J.W., 2005. Coupled plastic wave propagation and column buckling. *Journal of Applied Mechanics* 72 (1), 1–8]. At larger deformations, the material strain rate hardening contribution to the total energy is as pronounced as the contribution arising from microinertia effect. © 2006 Elsevier Ltd. All rights reserved.

* Corresponding author. Tel.: +1 847 467 5989; fax: +1 847 491 3915.
E-mail address: espinosa@northwestern.edu (H.D. Espinosa).

Keywords: Trusses; Sandwich structures; Dynamic compression; Inertia effect; Strain rate effect

1. Introduction

Materials combining lightweight and high mechanical energy absorption capability are of primary interest in a variety of structural designs including automobiles (crush resistance), microelectronics packaging (drop resistance), and ship hulls (dynamic loading). Metallic cellular materials are one such type of materials, which are promising and attractive for these applications (Gibson and Ashby, 1997). Cellular materials offer low densities and are highly efficient in absorbing mechanical energy from external loading. In the past decade, major advances were made in the design of cellular materials possessing periodic cellular topologies by exploiting minimum weight design, novel material fabrication processes, quasi-static and dynamic experimentation, and large-scale simulations.

Concerning the mechanical characterization of foam materials, especially at high rates of deformation, important contributions were made by Su and co-workers (1995a,b), Reid and Peng (1997), Harrigan et al. (1999), and Deshpande and Fleck (2000). These studies were mainly performed on foam materials with randomly distributed cells of random shapes. Since these investigations, new designs of topologically-structured metallic core materials have emerged (Evans et al., 1999, 2001). Two of these topologies are: (i) woven textile and (ii) truss cores. Metallic woven textile cores were developed by Sypeck and Wadley (2001), and Wadley (2002), and studied further by Zok et al. (2003), Wadley et al. (2003), and Zupan et al. (2004). Likewise, the high strain rate failure of metallic woven textiles materials was recently investigated by Lee et al. (2006).

Metallic truss cores with tetragonal topology were theoretically studied by Wicks and Hutchinson (2001, 2004). This work demonstrated that such cores possess an excellent combination of compressive strength and low weight. Experimental measurements and numerical simulations were also performed on the tetragonal and pyramidal truss cores as well as truss-cored sandwich panels by Deshpande and Fleck (2001), Sypeck and Wadley (2002), Chiras et al. (2002), Wadley et al. (2003), Rabczuk et al. (2004), Xue and Hutchinson (2004), Rathbun et al. (2004), and Zok et al. (2004). Whereas these truss cores were studied thoroughly by theoretical and numerical means, the performed experiments were limited to quasi-static loading.

To highlight the importance of investigating the dynamic compressive failure of metallic cores, which is the focus of this paper, we summarize here theoretical findings by Fleck and Deshpande (2004) in their investigation of sandwich panels with cellular cores. These authors formulated an analytical model to describe the overall deformation and strength of sandwich panels subjected to impulse loading. Their model suggested that the response of such structures can be separated into three main stages: (Stage I) impulse loading of front sheet; (Stage II) core compression phase and load transferring to back sheet; (Stage III) plate deflection and stretching (overall structural response). In Stage II, the compression of the core between the two face sheets is the dominant mechanism in energy absorption and, thus, core behavior plays a major role in overall sandwich plate performance under impulse loading. In this regard, one should note that compliant cores are desirable to minimize the impulse transmitted through the structure (fluid–structure interaction) but at the same time, the core must have enough compressive and shear strength to ensure

overall plate response. Therefore, understanding core behavior under a range of loading rates is essential in quantifying the response of sandwich panels.

This article presents results from experiments and simulations performed on stainless steel pyramidal truss cores at three different deformation rates. The article begins with a description of the pyramidal truss core material followed by a succinct description of the experimental techniques. Quasi-static compression tests were performed on a miniature-loading frame, intermediate strain rate compression tests were performed on a stored energy Kolsky bar, and high strain rate compression tests were performed using a light gas gun. Recorded nominal compressive stress–strain curves, at the various strain rates, are reported as well as real-time imaging of the specimen as obtained by means of high-speed digital photography. Specimen deformation, failure modes and their transition are then highlighted. In order to gain insight into the respective contributions of material strain rate hardening and structural inertia on the energy dissipation process, the partition of energy was analyzed using finite element models. The article closes with the main conclusions drawn from this investigation.

2. Experimental methodology

2.1. Pyramidal truss core materials

Sandwich panels with pyramidal truss cores made of 304 stainless steel were fabricated at the University of California at Santa Barbara following the fabrication technique reported by Sypeck and Wadley (2002), Wadley (2002), Wadley et al. (2003), and Rathbun et al. (2004). These consisted of two face sheets and a pyramidal truss core between these sheets as shown in Fig. 1. The thickness of the face sheets was 2.20 mm and that of the core was 11.65 mm. The core had a relative density, ρ^*/ρ_s (ratio between core density divided by that of the density of the solid material) of 3.5%. It was constructed with repeating pyramidal structures consisting of four truss struts, which had a square cross-section with a width of 1.18 mm. The span of one unit cell was $16.35 \times 15.88 \text{ mm}^2$.

This unit cell of the pyramidal structure repeated over the whole panel in the x - and y -directions; hence, in uniform compression, it can be assumed that the truss core sandwich panel behaves as the unit cell provided periodicity is achieved. In this paper, the compressive behavior of the unit cell is studied under a wide range of loading rates.

Using a unit cell might introduce degrees of freedom not present in a whole panel; for example, tilt of the face sheets, motion of the face sheets parallel to each other, or flexible

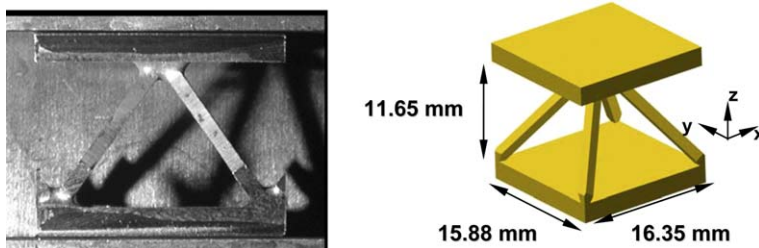


Fig. 1. 304 Stainless steel pyramidal truss core specimen (unit cell).

strut boundary conditions at the joints. To prevent these unwanted deformation modes, great amount of care was exercised in the preparation and conduction of experiments. Unit cell specimens were cut from the sandwich panel with extreme care by an abrasive saw at high RPM and very low feeding rate to avoid the tilt of the face sheets and avoid damage in the truss members. Extra brazing materials, which are stronger than the 304 SS, were left at the joints to maintain the periodicity of the structure by strongly attached trusses. The face sheets of the specimen were bonded to the loading platens by cyanoacrylate or epoxy before loading; thus, the motion of the face sheets in x - y plane perpendicular to the loading axis was restricted.

2.2. Quasi-static experimental set-up

The experimental setup for the quasi-static compression test, shown in Fig. 2, was used to achieve a strain rate of the order of 10^{-3} s^{-1} . The specimen was mounted between

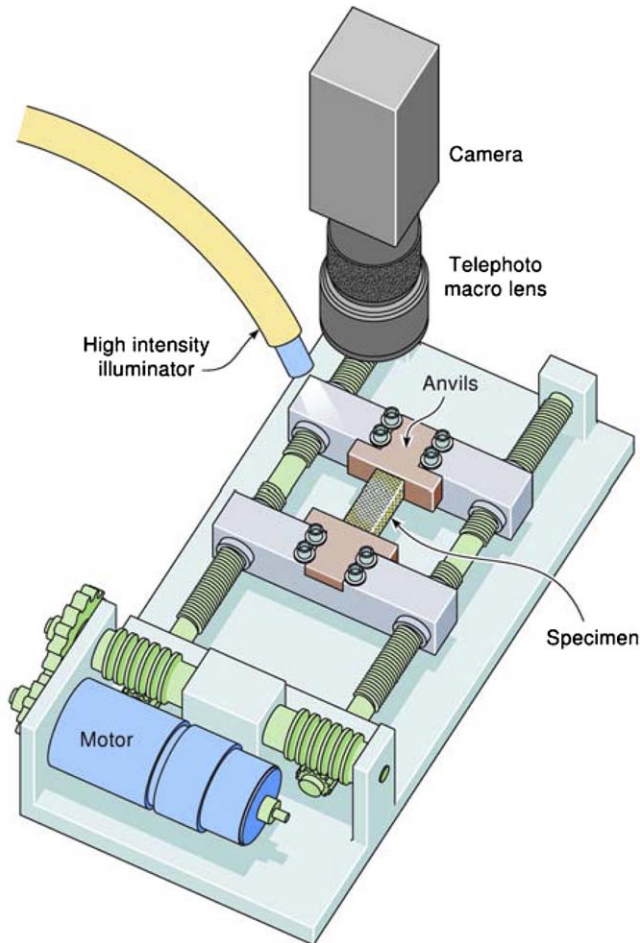


Fig. 2. Schematic of the quasi-static compression test setup.

compression platens in a miniature loading stage and positioned under a CCD camera equipped with a macro photographic lens. A load cell connected to a PC measured the compressive load and the load signal was recorded using LabVIEW software. The nominal stress was calculated by

$$\sigma_N(t) = F(t)/A_0, \quad (1)$$

where $F(t)$ is the measured force and A_0 is the initial cross-sectional area of the specimen, which is the rectangle spanning the four vertices of the pyramid. While the specimen was compressed, the load was recorded and sequential pictures of the deforming specimen were acquired synchronously to correlate the measurements of load and deformation. From the captured images, the relative displacement of the two face sheets was measured by digital image correlation (Chu et al., 1985). This measurement provided the average nominal strain over the specimen as,

$$\varepsilon_N(t) = \delta(t)/L_0, \quad (2)$$

where $\delta(t)$ is the measured relative displacement, and L_0 is the initial length of the specimen. This optical method avoided complications arising from machine compliance corrections and specimen edge effects.

2.3. Kolsky bar experimental set-up

Fig. 3 shows the stored-energy Kolsky bar apparatus used to perform dynamic experiments at nominal strain rates in the range of $100\text{--}1000\text{ s}^{-1}$. In this set-up an axial force was stored in the incident bar, between the hydraulic actuator and the clamp quick release device. Upon fracture of a pin in the clamp, an axial pulse traveling towards the specimen was generated. Following one-dimensional elastic wave theory, the axial force–time history of the specimen was computed from the strain history measured by a full Wheatstone bridge mounted on the surface of the transmitter pressure bar. The nominal stress was

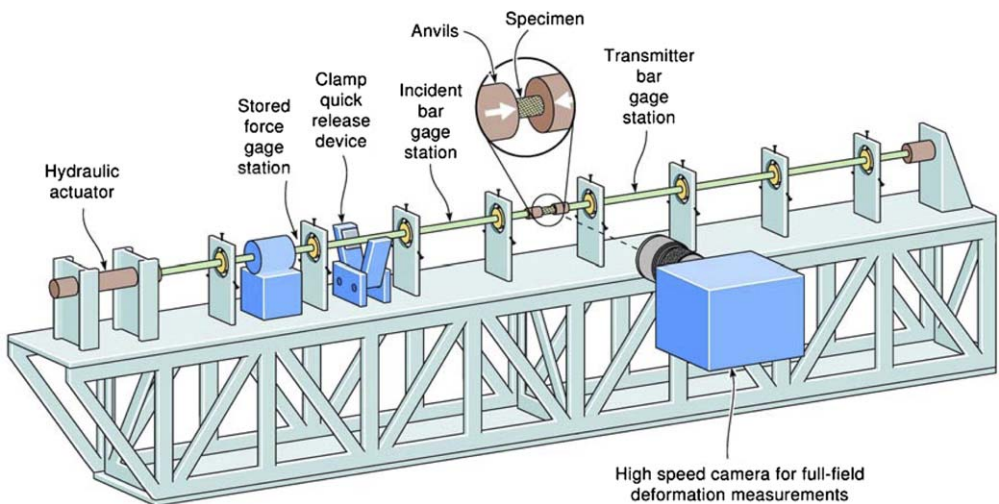


Fig. 3. Schematic of the Kolsky bar apparatus.

then computed directly from Eq. (1). The overall deformation of the specimen was calculated from the axial strain measured at the incident and transmitter bars at the gage stations shown in Fig. 3. The average nominal strain over the specimen was calculated directly by Eq. (2). A 8-CCD high-speed camera equipped with a long distance microscope was employed to capture eight images of deformation history of the specimen in a dynamic compression test. Two halogen white light sources illuminated the specimen continuously. Further details of this experimental setup can be found in Barthelat et al. (2003), and Lee et al. (2006).

2.4. Gas gun experimental set-up

Impact loading leading to higher nominal strain rates, up to 10^4 s^{-1} , were achieved using a 3" single stage gas gun apparatus (Fig. 4a), see Espinosa and Nemat-Nasser (2000). In the present study, a new set-up illustrated in Fig. 4(b) was developed to achieve higher deformation rates than in the Kolsky bar while using the exact same specimen geometry and allowing the same variables to be monitored (for details see Lee et al.,

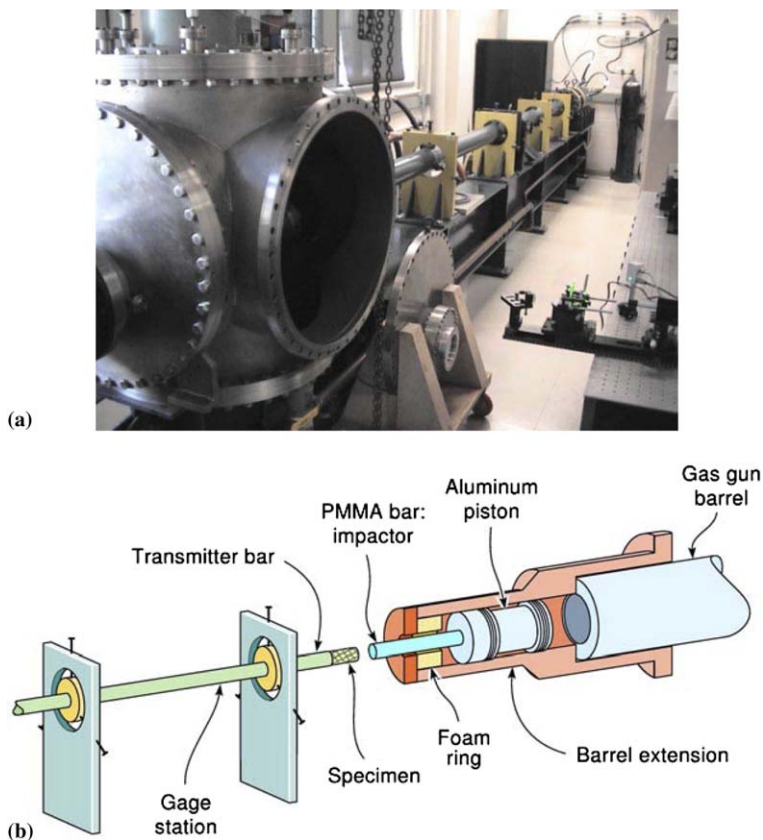


Fig. 4. (a) The light gas gun apparatus. (b) Schematic of direct impact tests and new configuration for bar-on-bar impact.

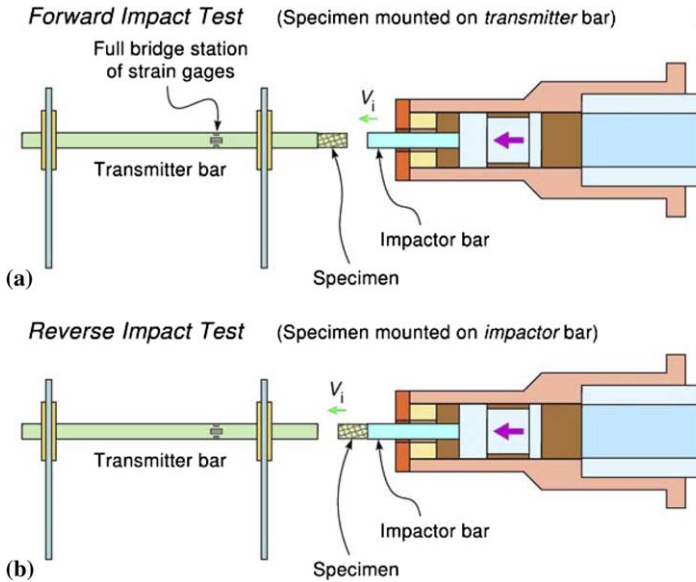


Fig. 5. Schematics of (a) forward impact test, which measures the load *ahead* of the shock wave, i.e., the load transmitted through the specimen and (b) reverse impact test, which measures the load *behind* the shock wave, i.e., the load applied to the specimen.

2006). In this set-up, an impactor bar, in lieu of the incident bar, was launched by the gas gun. The specimen was mounted either on the transmitter bar (*forward* impact tests, Fig. 5a) or on the PMMA impactor bar (*reverse* impact tests, Fig. 5b). Upon impact, a compressive pulse was generated in the specimen. This pulse propagated through the transmitter bar and was recorded using a strain gage station mounted on the transmitter bar. It was then used to compute the load history applied to the specimen.

In addition, optical measurements of projectile velocity and sample deformation rates were made in situ, by a laser line velocity sensor (LLVS). LLVS was originally developed by Ramesh and Kelkar (1995) and modified for this application such that the LLVS optics and photodetector are placed outside the target chamber (Lee et al., 2006). In this technique, we record the continuous and progressive blocking of a sheet of light by the impactor in front of the transmitter bar and above the specimen location. Additionally, the signal from the LLVS was used to trigger the high-speed camera. The images captured by the high-speed camera were used not only to identify deformation and failure modes, but also to estimate the impact and crushing velocity. The velocity was used to compute specimen displacements, which in turn yielded the nominal strain in the specimen. A 5 W diode pumped laser with a 2" beam expander was aimed at the specimen through the chamber window to provide diffuse and uniform illumination.

3. Experimental results

Uniform compression tests were performed on unit cell pyramidal truss core specimens. In quasi-static loading, the relative platen velocity was $8 \times 10^{-5} \text{ m s}^{-1}$, which corresponds to a strain rate of $7 \times 10^{-3} \text{ s}^{-1}$. The dynamic experiments in the Kolsky bar were performed

at a relative velocity of 2.5–6.4 m s⁻¹, which corresponds to a strain rate of 263–550 s⁻¹. In the gas gun, velocities of 84.5–115 m s⁻¹ were achieved, resulting in a nominal strain rate of about 7257–9875 s⁻¹. Fig. 6 is a plot of measured nominal stress–nominal strain signatures. In all cases, after an initial nominal stress increase, the load reaches a peak value and then drops. This load–displacement behavior is characteristic of structures prone to instability collapse. Buckling instability was observed with high-speed photography in all cases. A close examination of Fig. 6 reveals significant rate effects as manifested by differences in peak compressive nominal stress. The peak load in the gas gun loading is the largest, followed by the peak load measured in the Kolsky bar experiments, and as expected, the peak load measured in the quasi-static experiments was the smallest. In terms of nominal stress (F/A_0), the quasi-static peak stress is 4.0–4.2 MPa, about 60% the peak stress recorded in the Kolsky bar experiments (6.4 MPa) and three times smaller than the peak stress measured in the gas gun experiments (9.6–12.0 MPa).

In the quasi-static and Kolsky bar experiments, the post-peak load smoothly decreases to what seems to be a steady-state value, which is similar in both loading rates. On the other hand, several instabilities (load drops) at different displacement levels are recorded in the gas gun loading. Moreover, it is observed that the locations of the multiple load peaks depend on the specimens as inferred from comparison of experiments conducted at almost the same strain rate. Comparison of areas under load–deformation responses shows that the energy absorbed up to a strain of 0.4 in the gas gun experiment is more than twice the energy absorbed in the quasi-static and Kolsky bar experiments.

Differences in the failure modes were observed in the high speed recorded imaged. A comparison between quasi-static and Kolsky bar experiments is made in Fig. 7, which shows the nominal stress–strain curves for these cases together with a sequence of images at increasing nominal strains. In the quasi-static case, one or two plastic hinges developed at the center of each truss strut. All the truss members exhibited basically the same instability direction. By contrast, at a strain rate of 550 s⁻¹, each truss member had only one plastic hinge and the struts exhibited two different plastic buckling directions. The analysis of several Kolsky bar experiments revealed that the truss members could buckle in a variety of directions depending on their initial imperfections.

Examination of Fig. 8 reveals a major failure mode difference between the quasi-static/Kolsky and gas gun strain rates. At strain rates of 550 s⁻¹ and below, the truss members

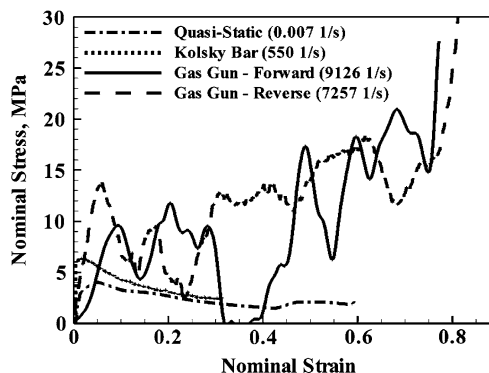


Fig. 6. Stress–strain curves of pyramidal truss core being crushed at different strain rates.

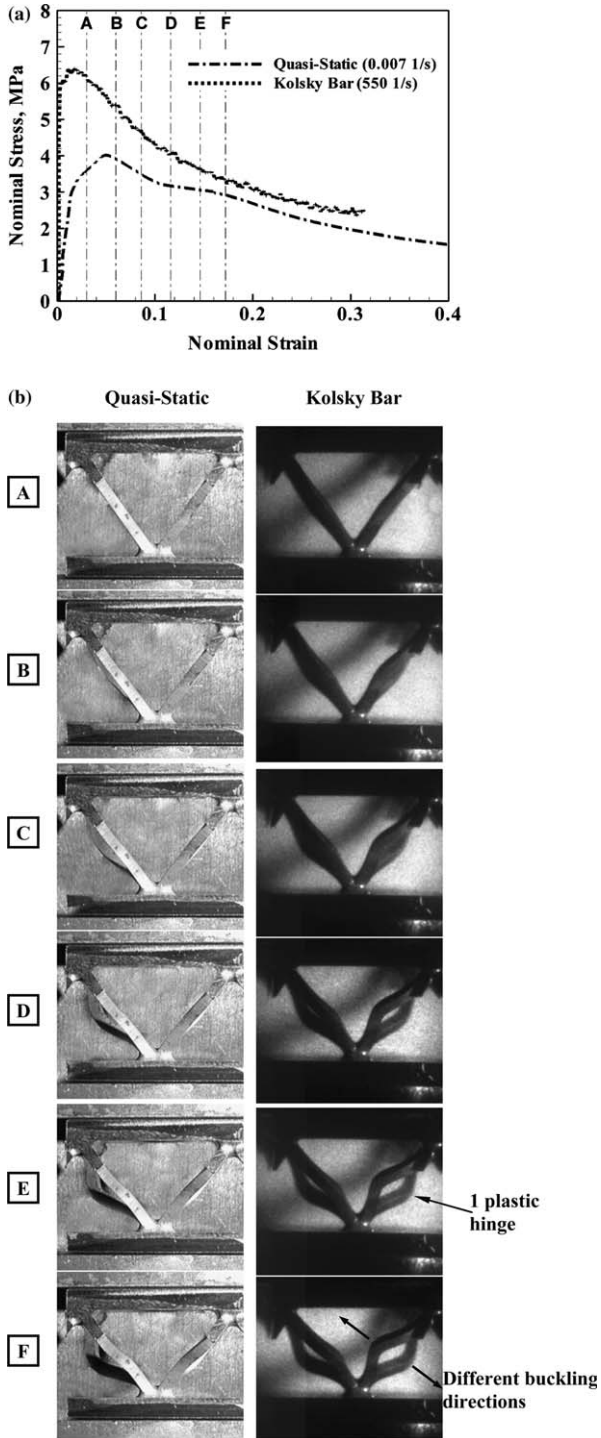
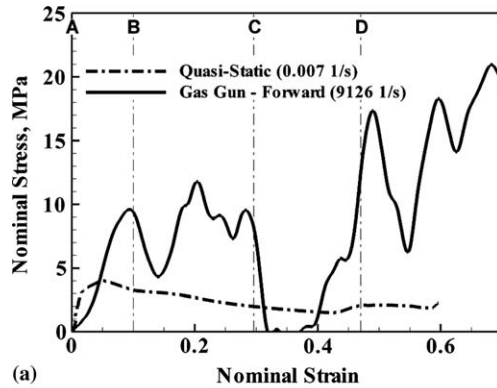
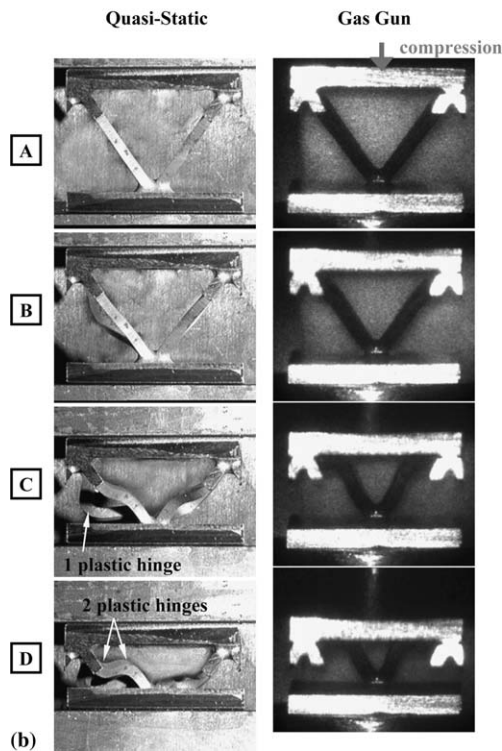


Fig. 7. (a) Comparison of stress–strain curves between quasi-static (0.007 s^{-1}) and Kolsky bar experiments (550 s^{-1}). (b) Comparison of failure modes between quasi-static (0.007 s^{-1}) and Kolsky bar experiments (550 s^{-1}).



(a)



(b)

Fig. 8. (a) Comparison of stress–strain curves between quasi-static (0.007 s^{-1}) and gas gun experiments (9126 s^{-1}). (b) Comparison of failure modes between quasi-static (0.007 s^{-1}) and gas gun experiments (9126 s^{-1}).

deformed laterally in a mode consistent with the buckling of fixed-fixed columns. By contrast, at nominal strain rates of about $1 \times 10^4 \text{ s}^{-1}$ the observed deformation mode was quite different, with the members deforming plastically in a more localized fashion. This is the case because propagation of the plastic wave delays overall buckling of the member (Vaughn et al., 2005). Hence, to achieve compatibility of deformation with the fast moving impacted sheet, the member needs to kink, as captured by the high speed photography. Careful inspection of the truss member deformation reveals that the buckling modes are

dependent on the initial member imperfections. In some cases, an anti-symmetric mode of buckling is observed. This is an important feature we will further address in the simulation section.

An interesting feature of the pyramidal truss topology is its stiffening beyond a certain nominal compressive strain. The reason for this stiffening is the contact of the deformed members with the face sheets. A further increase in energy absorption results from this mechanism. In quasi-static experiments, we have observed nominal stress–nominal strain curves showing four sudden increases in stiffness, which correspond to buckled legs making contact with one of the face sheets. The load becomes subsequently higher than the initial peak load. Similar features are observed in gas gun experiments where the samples are fully crushed (Fig. 8). In this case, the strain at which the stiffening occurs is smaller than the quasi-static case because the buckling configuration is quite different.

As pointed out by Vaughn et al. (2005) the magnitude of the axial compressive load or nominal compressive stress depends on the side where its magnitude is measured. To experimentally quantify this feature, we conducted reverse impact tests. In this configuration, one face sheet of the pyramidal truss core specimen was removed to avoid the high peak load associated with the impact of this plate to the stationary bar. Also, in this case the axial load (recorded by the gauge station mounted on the transmitter bar) is the one corresponding to the impact face rather than the load transmitted by the crushing specimen. Fig. 9 shows a comparison of nominal stress–nominal strain signatures between forward and reverse impact tests. Different nominal stress histories were observed with various differentiating features. In the reverse impact, the initial slope of the curve is steeper and the peak stress is about 30% higher than in the case of direct impact. At a strain of about 0.3, the reverse impact test shows a sudden increase of stress in contrast to the sudden stress drop recorded in the forward impact test. This is consistent with the effect of inertia and propagation of a plastic wave along the bars. It implies that the applied force is higher than the force transmitted through the specimen due to the force unbalance compensated by inertia. Examination of the failure sequence in the reverse impact, Fig. 9, shows a failure mode similar to that in the forward impact. An interesting feature observed in this experiment is that the pyramid apex is bouncing back, between frames at 75 and 100 μ s, as a result of the imparted kinetic energy.

4. Numerical modeling

Finite element simulations were performed to gain insight into the failure modes and the partition of energy between internal and kinetic as a function of deformation rate. Various details of the system are modeled to understand the contributions of microinertia and material rate dependence on the overall core performance. In this regard, we examine not only such effects on peak stress but also on the overall energy absorption process.

4.1. Finite element model

Three-dimensional quasi-static simulations were performed using ABAQUS/Standard while dynamic simulations were performed with ABAQUS/Explicit. In both cases eight-node brick elements with reduced integration were employed. The model is based on the actual geometry and dimensions of the tested pyramidal truss core. Due to symmetry, only a quarter of the unit cell was meshed (Fig. 10) for most of the simulations. A full

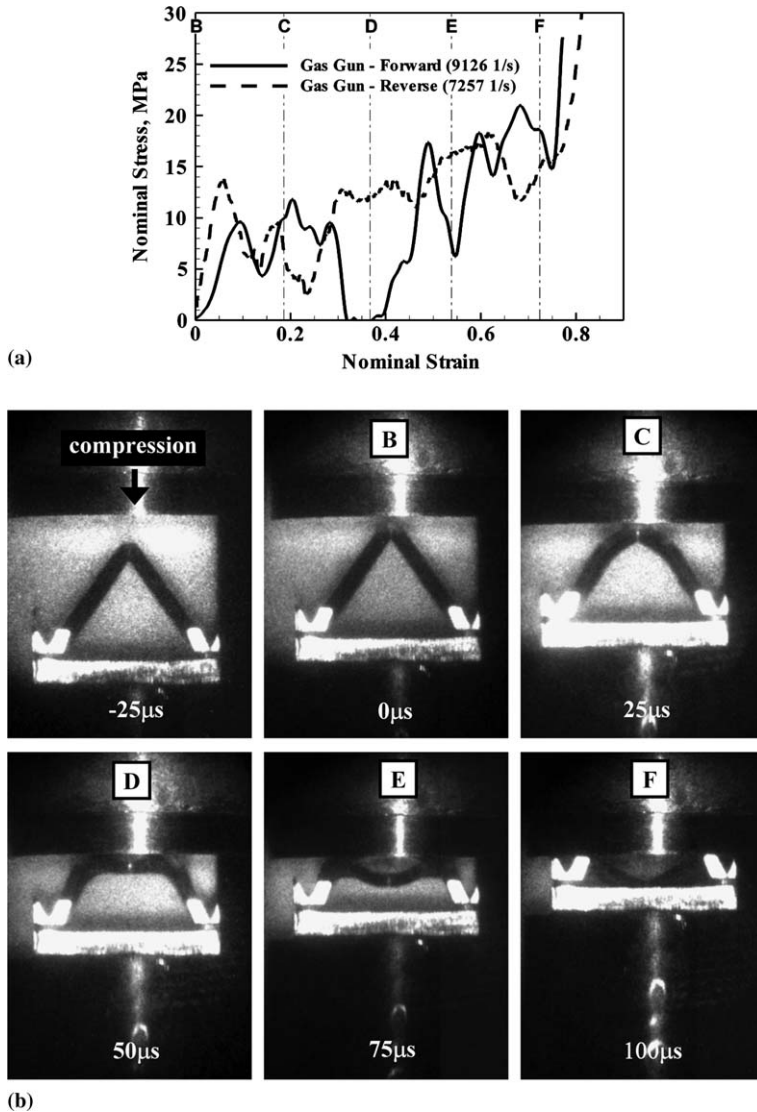


Fig. 9. (a) Comparison of stress–strain curves between forward and reverse impact tests. (b) A sequence of frames as taken in the reverse impact experiment.

model of the unit cell was used in certain cases as required. Contact elements were employed to account for contact between the members and the face sheets upon core crushing. One of the face sheets was subjected to a progressive displacement (quasi-static case) or to a suddenly imposed velocity (dynamic case) as in the experiments. The other face sheet was fixed in the loading direction. Symmetry and periodic boundary conditions were prescribed on the lateral faces of the cell.

In view that the properties of 304 stainless steel are sensitive to deformation and heat treatment histories, we performed quasi-static tests with specimens machined from the

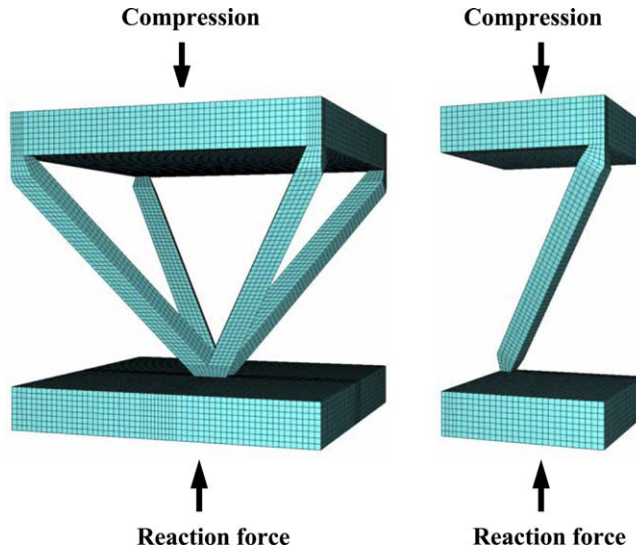


Fig. 10. Finite element models and meshes employed in the numerical simulations. A full model (left) and a quarter model (right).

truss members. The measured true stress–strain for the truss legs is shown in Fig. 11. It agrees very well with the constitutive behavior of annealed 304 stainless steel as reported in the literature (Washko and Aggen, 1990; Maloy et al., 2004), Fig. 11. This finding is obviously due to the fact that the final fabrication step of the truss core was brazing, which is similar to the annealing performed in these alloys (Syneck and Wadley, 2002; Rathbun et al., 2004). Therefore, it is reasonable to assume that the constitutive behavior of the truss core material is the same as that of annealed 304 stainless steel. Due to the small size of each truss leg, it was difficult to perform dynamic tensile or compression tests on such specimens utilizing the Kolsky bar or the gas gun setup. Hence, annealed 304 stainless steel specimens were tested in the Kolsky bar at the tensile strain rate of 508 s^{-1} . The dynamic

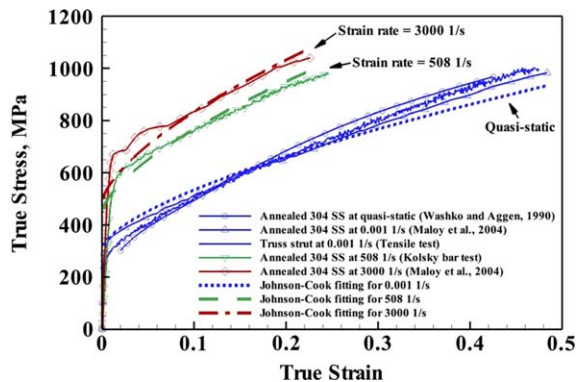


Fig. 11. Stress–strain behavior of truss leg and annealed 304 stainless steel, and fitting onto the Johnson–Cook constitutive model.

response of annealed 304 stainless steel at a strain rate of 3000 s^{-1} was reported by Maloy et al. (2004). Since the material behavior at rates of 508 and 3000 s^{-1} is adequate for our purpose, this dynamic material behavior was employed in our modeling. A summary of the experimental data is given in Fig. 11.

The Johnson–Cook model, which includes strain hardening, strain rate, and temperature effects, was used as a constitutive model in the simulations. According to this model, the flow stress σ_y is given by

$$\sigma_y = \left(A + B \left(\epsilon_p^{\text{eq}} \right)^n \right) (1 + c \ln \dot{\epsilon}^*) (1 - (T^*)^m), \quad \text{where } \dot{\epsilon}^* = \frac{\dot{\epsilon}_p^{\text{eq}}}{\dot{\epsilon}_0}, \quad (3)$$

$$T^* = \frac{T - T_{\text{room}}}{T_{\text{melt}} - T_{\text{room}}},$$

where ϵ_p^{eq} and $\dot{\epsilon}_p^{\text{eq}}$ are equivalent plastic strain and equivalent plastic strain rate, respectively. T is the material temperature, T_{room} is the room temperature, and T_{melt} is the melting temperature of the material. A , B , n , c , $\dot{\epsilon}_0$ and m are Johnson–Cook parameters determined by fitting to the experimental curves. The material properties and the identified Johnson–Cook parameters for the annealed 304 SS are listed in Table 1. To assess the temperature effect in the constitutive model, two different cases of simulations were performed: (a) without thermal coupling; (b) with thermal coupling. For the thermal analysis, adiabatic heating was assumed and 0.5 was used for the fraction of plastic dissipation rate converted into heat. The specific heat and thermal expansion coefficient for the 304 stainless steel were employed. The initial temperature condition was 298 K. Comparison of the results between the two cases showed no significant difference even for the case corresponding to deformation rates imposed in the gas gun experiments. Thus, all the simulations reported in this paper neglect the thermal effect.

4.2. Numerical results in the absence of geometric imperfections

A plot of nominal stress as a function of nominal strain, for the quasi-static case, showing both experimental record and numerical prediction, is given in Fig. 12. The FEA simulation captures the strain hardening region, peak stress, buckling and contact of leg and face sheet. The agreement is reasonable but the FEA model over-predicts the peak stress. In the experiments, the buckling behavior is highly dependent on the initial imperfection in each axial member as can be observed in the sequence of images capturing the deformation history. The frame corresponding to a nominal strain of 0.5 clearly shows that only the member at the lower back has one plastic hinge and is in contact with the right face sheet. As we will show later in the study of imperfections, the peak stress and buckling behavior are sensitive to initial geometrical defects in the members.

Table 1
Material properties and Johnson–Cook parameters of the annealed 304 SS

Density (kg/m^3)	Young's modulus (GPa)	Poisson's ratio	Melting temperature (K)	Room temperature (K)	Specific heat (J/kg K)
7900	200	0.3	1673	293	440
A (MPa)	B (MPa)	n	c	$\dot{\epsilon}_0$ (s^{-1})	m
310	1000	0.65	0.07	1.00	1.00

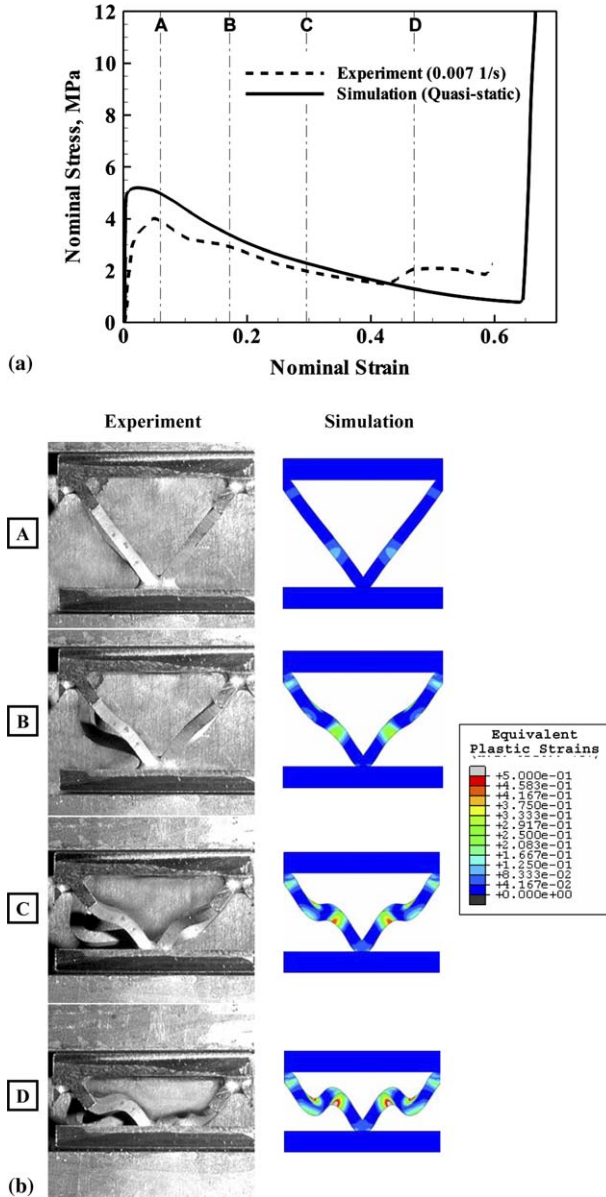


Fig. 12. (a) Stress–strain curves of experimental result and numerical simulation for quasi-static loading (0.007 s^{-1}). The FEA model does not include initial imperfections. (b) Failure modes in experimental result and numerical simulation for quasi-static loading (0.007 s^{-1}).

The reader should note that in the dynamic experiments, finite-size strain gages were used to record the axial force. The implication is that at any given time, non-uniform deformation fields are averaged over the length of the strain gage. Hence, when stress waves sweep the gage station a spatial averaging takes place. Such averaging was included

in the post-processing of the simulation results with the purpose of achieving a consistent comparison between simulation and experimental results.

When Kolsky bar experimental record and simulation are compared, it is observed that the numerical prediction follows the experimental results except for an overestimation of the peak stress, see Fig. 13. The real time images of the deformation and the FEA deformation prediction agree quite well overall. Again, the real time images captured with high speed photography show that the each member buckles in a different direction and by different amounts while in the simulation all members displace by the same amount due to the perfect symmetry of the model without imperfections.

For the case of the gas gun experiments, the recorded and simulated nominal stress–strain behavior show some noticeable discrepancies, see Fig. 14. The FEA predicts the overall trend of the stress–strain behavior but does not follow all the details such as several stress drops observed in the experimental signature. This is most noticeable during the post-buckling response, i.e., at strains larger than 0.5. We believed the origin of the discrepancy is the result of initial imperfections in the members and the non-simultaneous buckling of the four axial members. Likewise, in the experiments there might be a very slight tilt between impactor rod and sample face sheet. Such tilt can easily explain the difference in the slope of the signatures prior to the peak stress. Despite this initial difference in the stress history, the predicted peak stress is very similar in magnitude to the measured one. In addition, the simulation captures the buckling, at a strain of 0.3, and the drop in stress to a value of approximately zero. Moreover, the deformation patterns are strikingly similar.

In the following subsections, we examine each one of the observed discrepancies by enhancing the model to account for the additional features observed in the real system.

4.3. Imperfection effects

Plastic buckling of the truss struts is the dominant failure mechanism in the compression of the truss core, especially in the cases of quasi-static and Kolsky bar tests, where the inertia effect is negligible or very small. Hence, it is clear that an initial imperfection in the structure would play a significant role in the overall failure behavior. To assess the effect of initial imperfections, a geometric imperfection was introduced in the model following the preferred direction of buckling as captured in the experiments. The initial imperfection of the truss structure was introduced by slightly deflecting a truss strut in the transverse direction to the truss axis. The deflection shape is sinusoidal to satisfy compatibility of deformation at the joint and the amplitude is determined by a fraction of the thickness of the truss strut, namely,

$$\psi = \alpha \frac{t_t}{2} \left(1 - \cos \frac{2\pi\xi}{L_t} \right), \quad 0 \leq \xi \leq L_t, \quad (4)$$

where α is the normalized maximum deflection on the center, t_t is the truss strut thickness (1.18 mm), and L_t is the truss strut length (16.3 mm).

Fig. 15 shows the directions of the local coordinate system (ξ , ψ , ζ), used in defining the initial imperfections. L_t was measured between two points laying on the intersections of the symmetry planes of the quarter model and the interfaces between the truss strut and face sheets. The local coordinate ξ is oriented along the line L_t defining the strut axis, and ψ , perpendicular to ξ , lays on the plane defined by the line L_t and the diagonal of

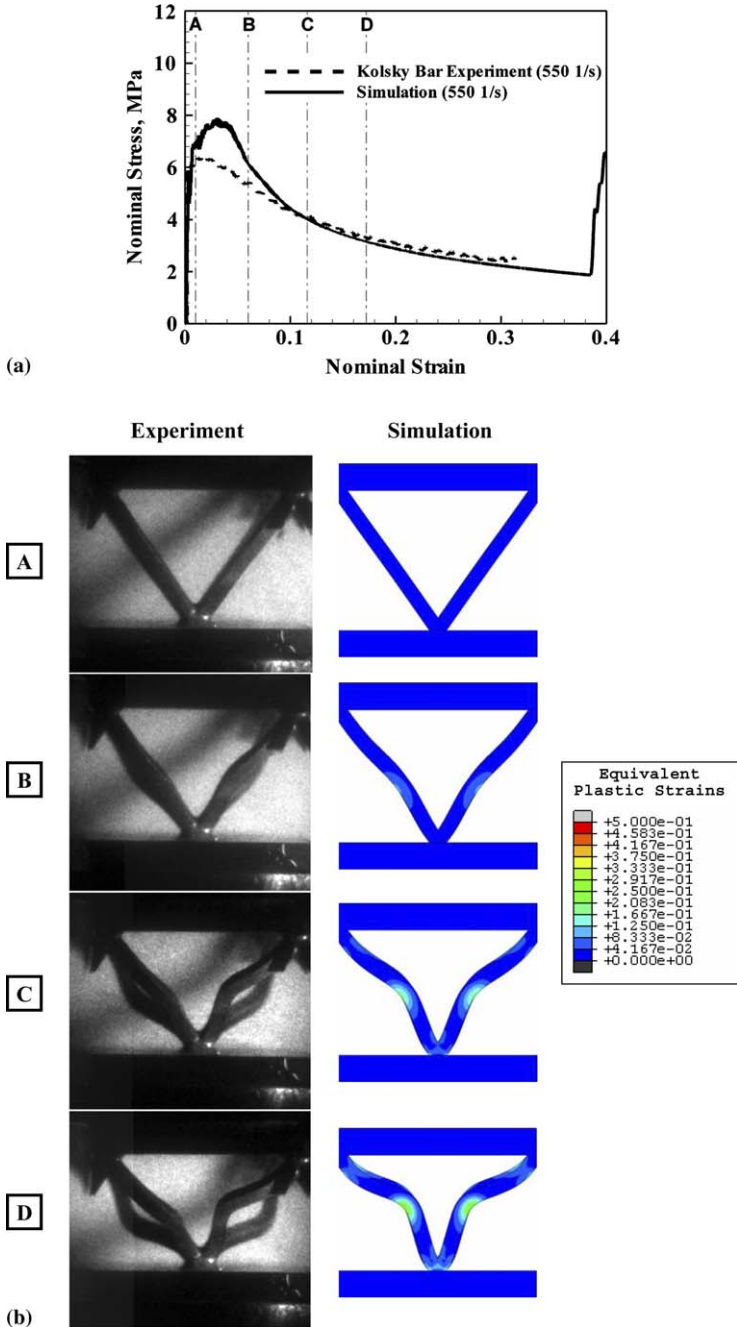


Fig. 13. (a) Stress–strain curves of experimental result and numerical simulation for Kolsky bar loading (550 s^{-1}). The FEA model does not include initial imperfections. (b) Failure modes in experimental result and numerical simulation for Kolsky bar loading (550 s^{-1}).

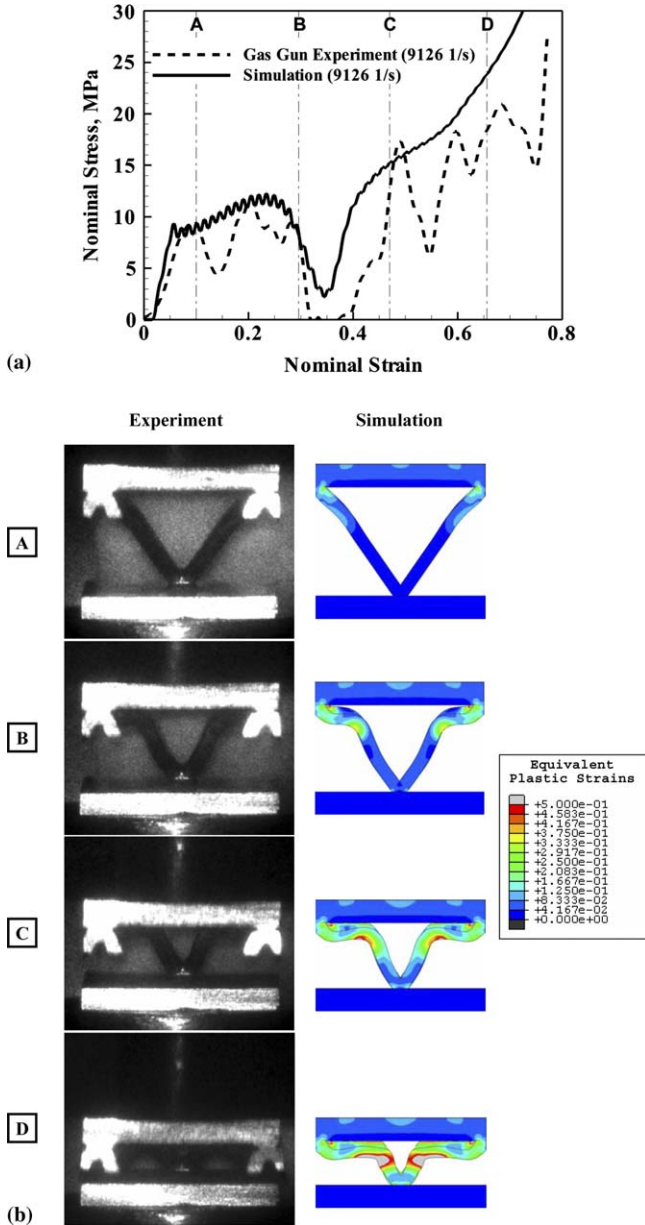


Fig. 14. (a) Stress–strain curves of experimental result and numerical simulation for gas gun loading (9126 s^{-1}). The FEA model does not include initial imperfections. (b) Failure modes in experimental result and numerical simulation for gas gun loading (9126 s^{-1}).

the face sheet plane connected to the line L_t . In the following simulations, α was set to 5% (0.059 mm).

Fig. 16 shows the quasi-static simulation results of the truss cores with initial imperfections in two directions (I and II). From the computed stress–strain curves, it is noted that

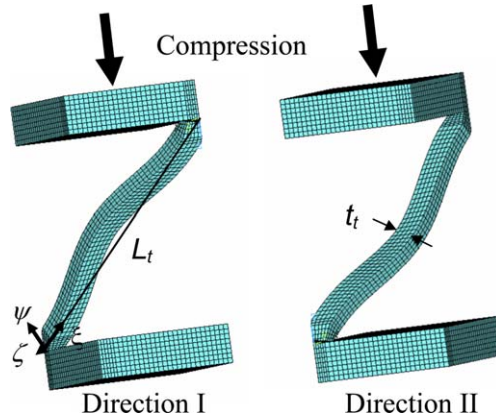


Fig. 15. Initial geometric imperfection in the truss struts ($\alpha = 1.00$ for direction I; $\alpha = -1.00$ for direction II).

the peak stress level in the cases with imperfection is lower than in the case without imperfection. A sudden stress increase is observed at a later stage of deformation, in both experiments and simulations. As previously mentioned, this is the case because the buckled truss strut makes contact with the face sheet. The simulation without imperfection predicts such contact at a nominal strain of 0.65, while the experiment recorded the increase at 0.43. For the model with initial imperfection the truss-face sheet contact takes place much earlier, namely, at a strain of 0.37. Interestingly, it is found that imperfect truss struts have only one plastic hinge in the middle of the strut length, while the perfect truss struts have two plastic hinges as the buckling progresses. As highlighted in the discussion of Fig. 12, different buckling directions are observed in the experiments for the various truss members. Hence, the direction of the initial imperfection determines the direction of the buckling. However, based on the fact that the force is equilibrated on the two face sheets and the unit cell is periodically repeated, the two cases with initial imperfections in direction I and direction II are basically identical models. Consequently, the stress–strain curves of those cases are the same and the failure shapes are mirrored images to each other.

Similar features can be observed in the simulation results with imperfections for the Kolsky bar loading case, see Fig. 17. The peak stress decreases and takes place at a smaller nominal strain than in the case without imperfection. However, it is important to note that the overall trends after the peak stress are not dependent on the imperfection and agree well with experimental results. As in the quasi-static case, the initial imperfection triggers a sudden increase of stress upon strut-face sheet contact, at a strain of 0.35, which is earlier than in the case of no imperfection. Regardless of the imperfection, only one plastic hinge forms in all cases but the direction of the buckling is dependent on the direction of the initial imperfection. Note that at this moderate strain rate (Kolsky bar testing), the force equilibrium is rapidly achieved after a short transient so that the two different directions of the imperfection yield almost the same results but they are not necessarily identical.

In the simulations of the gas gun experiments we found that the peak stress is insensitive to the imperfection, as shown in Fig. 18. However, the instability occurred earlier and more abruptly in the case of imperfection in direction I and the hardening is steeper after the truss members makes contact with the face sheet at a nominal strain of about 0.4. The model with imperfection in direction II shows delayed instability to a nominal strain of

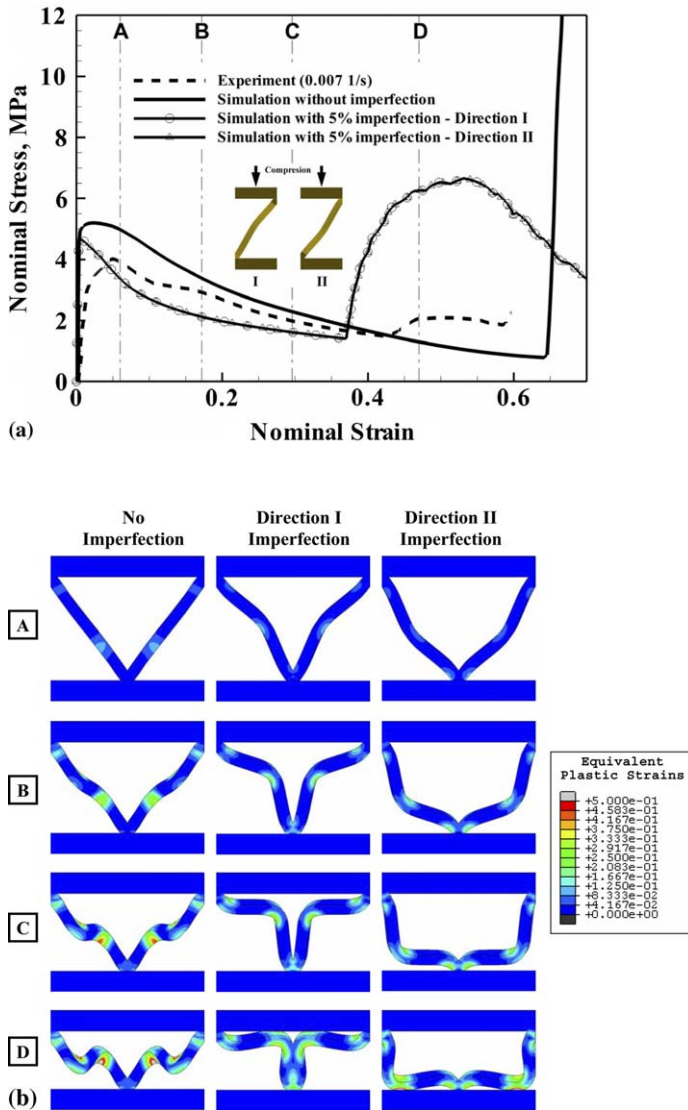


Fig. 16. Effect of initial imperfection on failure behavior of truss core in quasi-static loading case (0.007 s^{-1}). (a) Stress–strain curves. (b) Sequence of failure modes.

about 0.3 and it exhibits softening after a strain level of 0.5, which is closer to the experimental result. When the failure patterns are examined, their difference is hardly noticeable.

To capture more details of the experimental stress–strain curves, full models of the truss core unit cell were examined with all four struts and different numbers of imperfect struts, Fig. 19. Each imperfect strut had an imperfection magnitude of 5% as above. It was found that the full-model simulation results were very close to the superposition of stress–strain behavior of four corresponding quarter models. Fig. 20 shows the stress–strain curves of

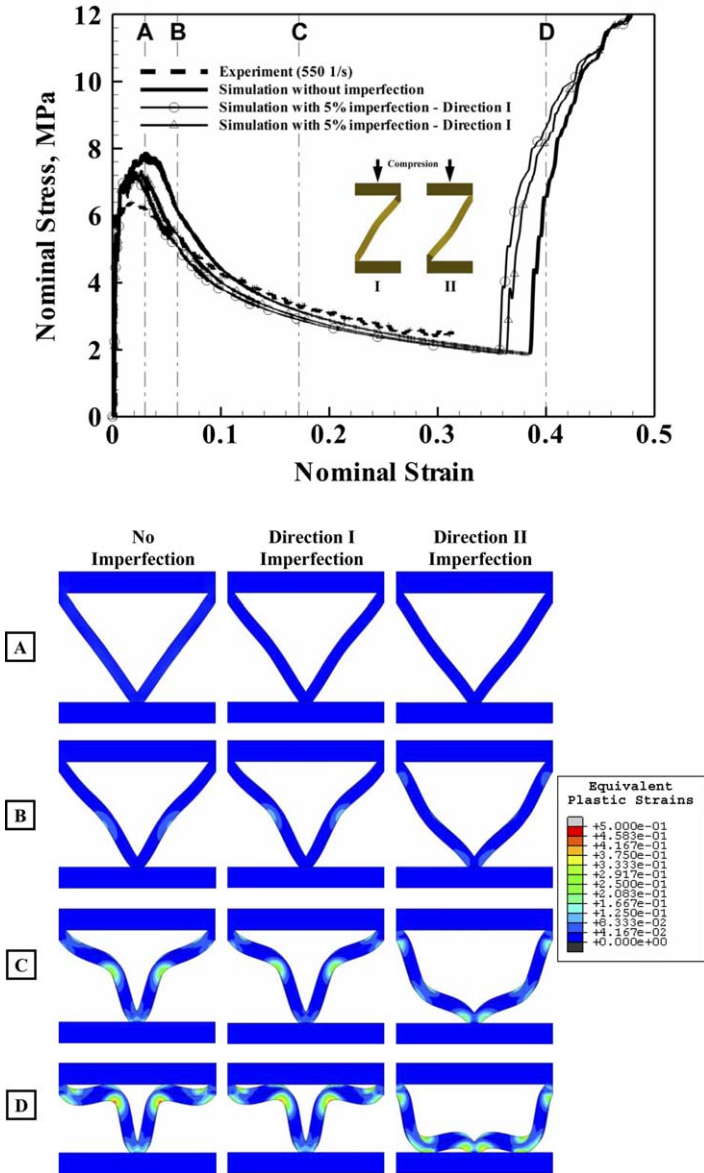


Fig. 17. Effect of initial imperfection on failure behavior of truss core in Kolsky bar loading case (550 s^{-1}). (a) Stress–strain curves. (b) Sequence of failure modes.

the full models in Kolsky bar loading. For instance, the responses of the case 2-A (symmetric) and the case 2-B (anti-symmetric) fall in the middle of the cases without imperfection and with four imperfections. Fig. 21 shows the full-model simulation results for the gas gun loading case. The stress–strain curve of the case 2-B (anti-symmetric) follows that of the case without imperfection as it may be obtained by superimposing the stress–strain

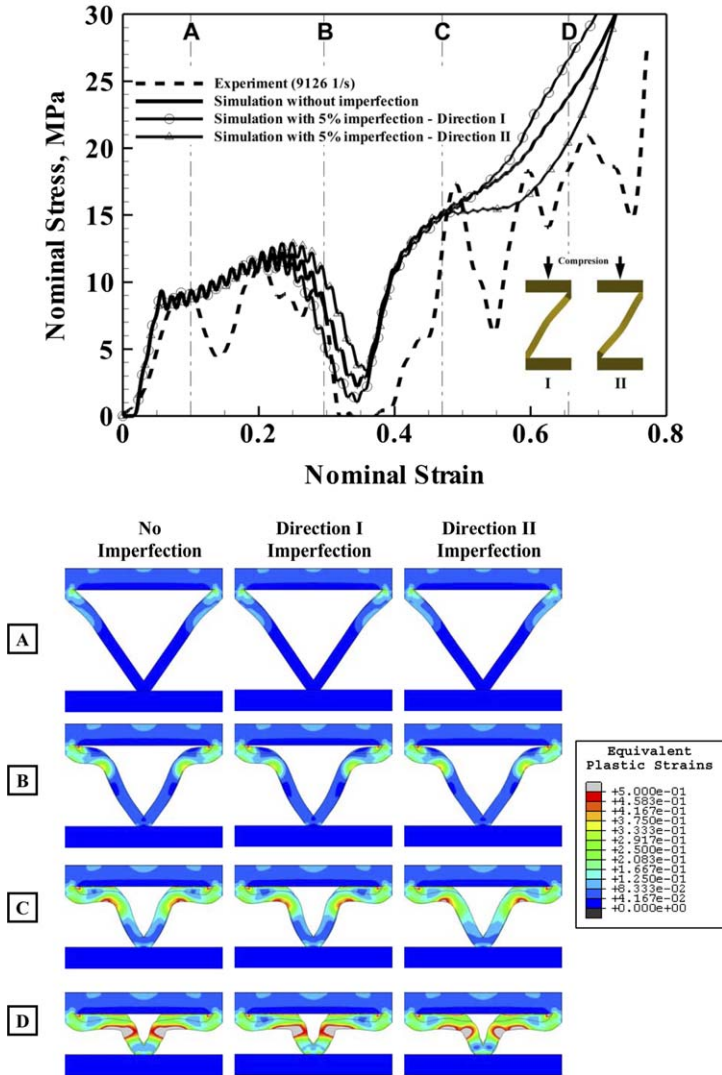


Fig. 18. Effect of initial imperfection on failure behavior of truss core in gas gun loading case (9126 s^{-1}). (a) Stress–strain curves. (b) Sequence of failure modes.

behaviors of one quarter model with imperfection direction I, one quarter model with imperfection direction II, and two quarter models without imperfection.

4.4. Effect of misalignment in the impact surfaces

In compression tests, even slight misalignment between the specimen surface and the loading platen can affect the load–displacement curve, especially in the initial stage. Despite significant care on specimen–impactor alignment, there is a possibility for a misalignment of a fraction of a degree to take place in the experiments. To estimate the effect

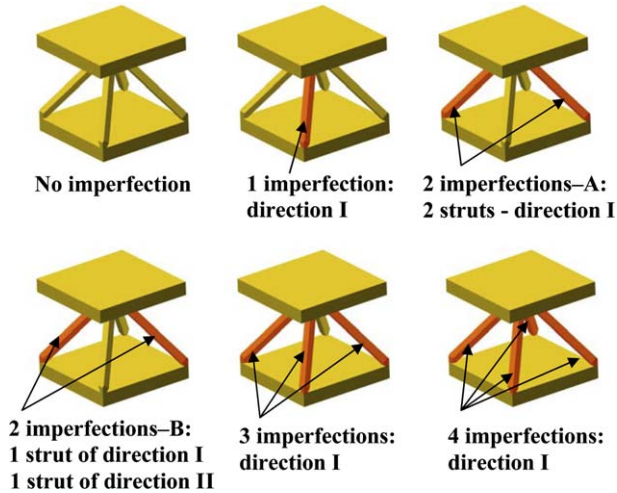


Fig. 19. Full models of four truss struts with different numbers of imperfect struts.

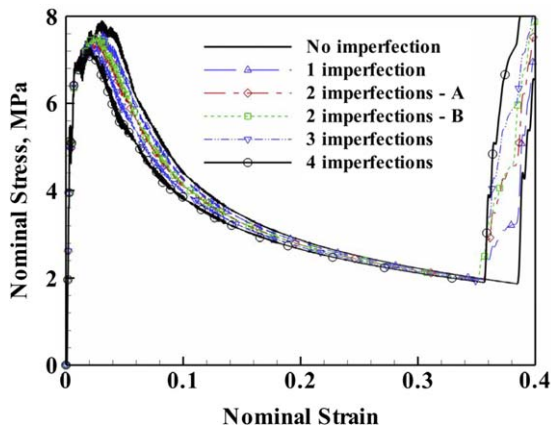


Fig. 20. Effect of different imperfections on failure behavior of truss core in Kolsky bar loading case (550 s^{-1}).

of misalignment in the impact surfaces, a small angle between the top face sheet of the specimen and the loading boundary condition was introduced in the gas gun simulations. In this case, a full model with four truss struts was employed. The velocity boundary condition was imposed on each node on the top face sheet at the moment when the tilted impactor surface made contact with that node. Fig. 22 shows the nominal stress–strain curve resulting from a model with 1.5° tilt. The model with misalignment captured the trends of the recorded nominal stress–strain behavior. Indeed, the initial slope was predicted quite well and the stress–strain curve followed the measured curve up to the peak stress. The hardening at large strains is smaller than for the model without misalignment. We should mention that we incorporated both the imperfections and the misalignment in one full model but no significant coupled effect was observed.

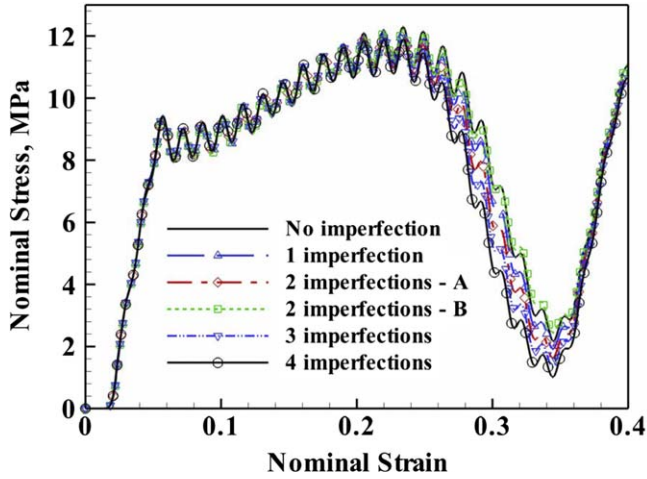


Fig. 21. Effect of different imperfections on failure behavior of truss core in gas gun loading case (9126 s^{-1}).

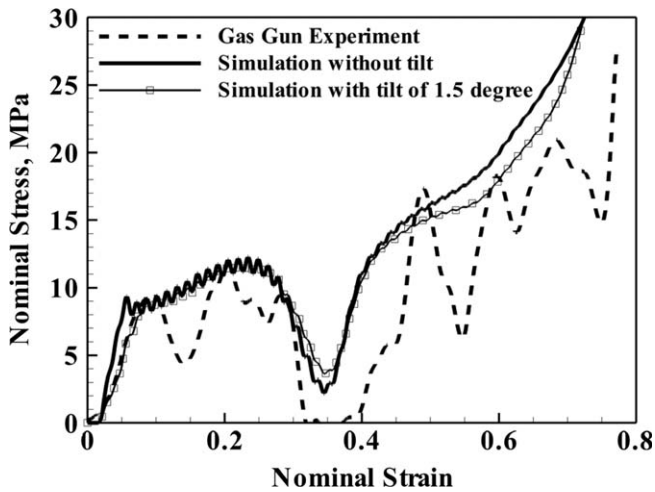


Fig. 22. Effect of misalignment of impact surfaces on failure behavior of truss core in gas gun loading case (9126 s^{-1}).

4.5. Energy partition during the crushing process

With the accuracy and predictive capability of the FEM model established, the fundamental question of how the energy is partitioned during the core crushing can be examined. In particular, an assessment of the role of material strain rate versus microinertia in the post-buckling behavior is quantified. Based on the FEM model, energy absorption is compared between the three cases: quasi-static, Kolsky bar, and gas gun loading rates. According to the energy conservation principle, the external work delivered to the specimen is equal to the sum of kinetic energy and internal energy including both strain hardening and strain rate hardening effects. The total external energy, internal energy and

kinetic energy were computed following customary continuum mechanics formulations and their numerical implementations. Fig. 23 is a plot of these energies for the various simulated cases. Significant rate effects on the total energy are predicted in the gas gun case. As expected rate effects are quite moderate in the Kolsky bar case. This implies that rate effects become important only at the deformation rates imposed by the gas gun. Examination of Fig. 23 reveals that the kinetic energy in the Kolsky bar case is negligibly low in comparison with the total energy.

To assess the material strain rate hardening and inertia effects separately, the gas gun simulation was performed without material strain rate hardening by removing the contribution in the Johnson–Cook constitutive model, i.e., $c = 0$ in Eq. (3). The outcome of these calculations is also shown in Fig. 23. By comparing the simulation results without material strain rate hardening to that with rate hardening, at a nominal strain of about 0.3, it is observed that the internal energy decreases by a significant amount, which can be attributed to the contribution of material strain rate hardening to the energy absorption. The specimen deformation mode hardly shows any difference from that with strain rate hardening. Similarly, the kinetic energy in the case of no strain rate hardening is

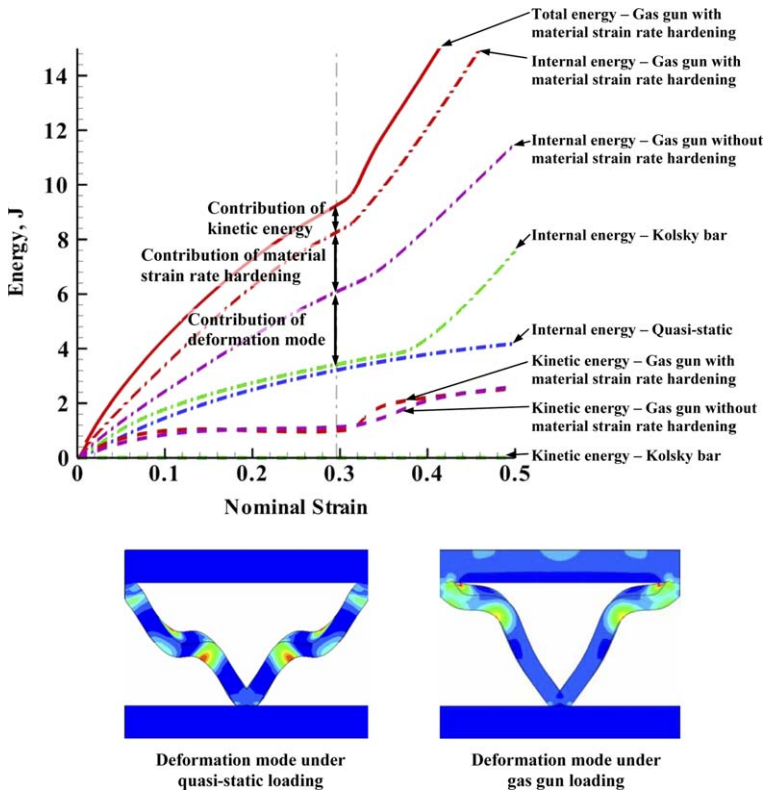


Fig. 23. Energy absorption in a unit cell subject to different deformation rates. The lower images are deformation predictions at 0.296 nominal strain for the two cases: quasi-static (0.007 s^{-1}) and gas gun loading cases (9126 s^{-1}). These images show the differences in the deformation of the trusses as a result of strain rate and inertia effects. (1) contribution of microinertia; (2) contribution of material strain rate hardening; (3) contribution of deformation mode.

almost the same to that with strain rate hardening. Comparing the internal energy stored in the gas gun case without strain rate hardening and that of the quasi-static case at a nominal strain of 0.3, it is realized that the difference is due to the difference in deformation mode because both models exhibit no strain rate hardening effect. Microinertia causes plastic wave propagation in the axial direction (Vaughn et al., 2005) and affects the lateral deflection during the buckling. The result is a major difference in failure mode as shown in Fig. 23. The contribution of the failure mode in the gas gun case is even larger than that of kinetic energy or material strain rate hardening.

These findings are consistent with the inertia-induced rate effect of a specific type of structure, reported by Calladine and English (1984), Tam and Calladine (1991), and Su and co-workers (1995a,b). The so-called “type II” structure exhibits an increase in strength with deformation rate and they proposed that inertia effects are a significant contribution to this rate effect even when the strain rate sensitivity of the material is ignored.

5. Conclusions

The compressive behavior of a pyramidal truss core was investigated under various strain rates ranging from 10^{-3} s^{-1} (quasi-static) to $10^2\text{--}10^3 \text{ s}^{-1}$ (Kolsky bar), and up to 10^4 s^{-1} (gas gun). Quasi-static tests were performed using a miniature loading frame. A stored energy Kolsky bar was used for intermediate strain rates, while a light gas gun was used for direct and reverse impact of the specimens. Real time deformation observations were performed for all three test types. A digital CCD camera was used in quasi-static experiments and a high speed CCD camera was employed in the dynamic experiments. The deformation modes were identified from the images and investigated in detail.

The compressive behavior of the pyramidal truss core was further investigated by means of finite element simulations using a Johnson–Cook material model. The overall features of the numerically predicted nominal stress–strain curves agree reasonably well with those experimentally recorded. The simulations successfully captured the distinct deformation modes at the three tested regimes of deformation. It is also found that when initial imperfections and impact misalignment are included in the numerical model, the simulations capture the more subtle features recorded in the experiments. Even when the simulations did not follow the nominal stress–strain records in every single detail, it was demonstrated that initial imperfections and tilt can explain the observed features. Hence, it is reasonable to state that using an inverse method with enough degrees of freedom, the stress–strain signatures can be reproduced as accurately as desired. Such endeavor is beyond the scope of this work. However, we believe that pursuing more accurate reconstruction of the measured signatures would not change the energy partitions and the main conclusions.

By examining the partition of energy at various crushing stages, it was observed that at the early stages of deformation, the kinetic energy (microinertia) plays a more dominant role than in the post-buckling regime. Microinertia appears as a dominant effect in determining the peak nominal stress. A coupling between plastic wave propagation (controlled by axial inertia) and buckling by lateral displacement were experimentally observed and numerically predicted. At strain rates of the order of $1 \times 10^4 \text{ s}^{-1}$, a very unique deformation of the members arises from deformation compatibility. Members crush against the fast moving face sheet and make contact early in the crushing process. This finding is in agreement with the in-depth quantification of the role of microinertia on peak stress

carried out by Vaughn et al. (2005). Examination of the pyramidal truss core energy absorption at larger deformations, e.g., at a nominal strain of 0.3, reveals that the material strain rate hardening contribution to the total energy is as pronounced as the contribution arising from microinertia effect.

Acknowledgements

The authors express their special thanks to Professors A.G. Evans and F. Zok, R. McMeeking and Dr. H. Rathbun from University of California at Santa Barbara for their aid in the fabrication of samples and insightful discussions during the investigation reported here. This work was sponsored by the Office of Naval Research under Award No. 123163-02-N00014-02-1-0700.

References

- Barthelat, F., Wu, Z., Prorok, B.C., Espinosa, H.D., 2003. Dynamic torsion testing of nanocrystalline coatings using high-speed photography and digital image correlation. *Experimental Mechanics* 43 (3), 331–340.
- Calladine, C.R., English, R.W., 1984. Strain rate and inertia effects in the collapse of two types of energy-absorbing structures. *International Journal of Mechanical Sciences* 26, 689–701.
- Chiras, S., Mumm, D.R., Evans, A.G., Wicks, N., Hutchinson, J.W., Dharmasena, K., Wadley, H.N.G., Fichter, S., 2002. The structural performance of near-optimized truss core panels. *International Journal of Solids and Structures* 39 (15), 4093–4115.
- Chu, T.C., Ranson, W.F., Sutton, M.A., Peters, W.H., 1985. Application of digital-image-correlation techniques to experimental mechanics. *Experimental Mechanics* 25, 232–244.
- Deshpande, V.S., Fleck, N.A., 2000. High strain rate compressive behavior of aluminium alloy foams. *International Journal of Impact Engineering* 24, 277–298.
- Deshpande, V.S., Fleck, N.A., 2001. Collapse of truss core sandwich beams in 3-point bending. *International Journal of Solids and Structures* 38 (36–37), 6275–6305.
- Espinosa, H.D., Nemat-Nasser, S., 2000. Low-velocity Impact Testing. *ASM Handbook*, vol. 8. Ohio ASM International, Materials Park, pp. 539–559.
- Evans, A.G., Hutchinson, J.W., Ashby, M.F., 1999. Multifunctionality of cellular metal systems. *Progress in Materials Science* 43 (3), 171–221.
- Evans, A.G., Hutchinson, J.W., Fleck, N.A., Ashby, M.F., Wadley, H.N.G., 2001. The topological design of multifunctional cellular metals. *Progress in Materials Science* 46 (3–4), 309–327.
- Fleck, N.A., Deshpande, V.S., 2004. The resistance of clamped sandwich beams to shock loading. *Journal of Applied Mechanics* 71, 386–401.
- Gibson, L.J., Ashby, M.F., 1997. *Cellular Solids, Structure and Properties*, second ed. Cambridge University Press, Cambridge, UK.
- Harrigan, J.J., Reid, S.R., Peng, C., 1999. Inertia effects in impact energy absorbing materials and structures. *International Journal of Impact Engineering* 22 (9–10), 955–979.
- Lee, S., Barthelat, F., Moldovan, N., Espinosa, H.D., Wadley, H.N.G., 2006. Deformation rate effects in failure modes of open-cell Al foams and textile cellular materials. *International Journal of Solids and Structures* 43 (1), 53–73.
- Maloy, S.A., Gray III, G.T., Cady, C.M., Rutherford, R.W., Hixson, R.S., 2004. The influence of explosive-driven “Taylor-Wave” shock prestraining on the structure/property behavior of 304 stainless steel. *Metallurgical and Materials Transactions A – Physical Metallurgy and Materials Science* 35 (9), 2617–2624.
- Rabczuk, T., Kim, J.Y., Samaniego, E., Belytschko, T., 2004. Homogenization of sandwich structures. *International Journal for Numerical Methods in Engineering* 61 (7), 1009–1027.
- Ramesh, K.T., Kelkar, N., 1995. Technique for the continuous measurement of projectile velocities in plate impact experiments. *Review of Scientific Instruments* 66 (4), 3034–3036.
- Rathbun, H.J., Wei, Z., He, M.Y., Zok, F.W., Evans, A.G., Sypeck, D.J., Wadley, H.N.G., 2004. Measurement and simulation of the performance of a lightweight metallic sandwich structure with a tetrahedral truss core. *Journal of Applied Mechanics – Transactions of the ASME* 71 (3), 368–374.

- Reid, S.R., Peng, C., 1997. Dynamic uniaxial crushing of wood. *International Journal of Impact Engineering* 19, 531–570.
- Su, X.Y., Yu, T.X., Reid, S.R., 1995a. Inertia-sensitive impact energy-absorbing structures. Part I: effects of inertia and elasticity. *International Journal of Impact Engineering* 16 (4), 651–672.
- Su, X.Y., Yu, T.X., Reid, S.R., 1995b. Inertia-sensitive impact energy-absorbing structures. Part II: effects of strain rate. *International Journal of Impact Engineering* 16 (4), 673–689.
- Sypeck, D.J., Wadley, H.N.G., 2001. Multifunctional microtruss laminates: textile synthesis and properties. *Journal of Materials Research* 16 (3), 890–897.
- Sypeck, D.J., Wadley, H.N.G., 2002. Cellular metal truss core sandwich structures. *Advanced Engineering Materials* 4 (10), 759–764.
- Tam, L.L., Calladine, C.R., 1991. Inertia and strain-rate effects in a simple plate-structure under impact loading. *International Journal of Impact Engineering* 11 (3), 349–377.
- Vaughn, D., Canning, M., Hutchinson, J.W., 2005. Coupled plastic wave propagation and column buckling. *Journal of Applied Mechanics* 72 (1), 1–8.
- Wadley, H.N.G., 2002. Cellular metals manufacturing. *Advanced Engineering Materials* 4 (10), 726–733.
- Wadley, H.N.G., Fleck, N.A., Evans, A.G., 2003. Fabrication and structural performance of periodic cellular metal sandwich structures. *Composites Science and Technology* 63, 2331–2343.
- Washko, S.D., Aggen, G., 1990. Wrought Stainless Steels, 10th ed. ASM Handbook, vol. 1. Ohio ASM International, Materials Park, pp. 841–907.
- Wicks, N., Hutchinson, J.W., 2001. Optimal truss plates. *International Journal of Solids and Structures* 38 (30–31), 5165–5183.
- Wicks, N., Hutchinson, J.W., 2004. Performance of sandwich plates with truss cores. *Mechanics of Materials* 36 (8), 739–751.
- Xue, Z.Y., Hutchinson, J.W., 2004. Constitutive model for quasi-static deformation of metallic sandwich cores. *International Journal For Numerical Methods In Engineering* 61 (13), 2205–2238.
- Zok, F.W., Rathbun, H.J., Wei, Z., Evans, A.G., 2003. Design of metallic textile core sandwich panels. *International Journal of Solids and Structures* 40 (21), 5707–5722.
- Zok, F.W., Waltner, S.A., Wei, Z., Rathbun, H.J., McMeeking, R.M., Evans, A.G., 2004. A protocol for characterizing the structural performance of metallic sandwich panels: Application to pyramidal truss cores. *International Journal of Solids and Structures* 41 (22–23), 6249–6271.
- Zupan, M., Deshpande, V.S., Fleck, N.A., 2004. The out-of-plane compressive behavior of woven-core sandwich plates. *European Journal of Mechanics A – Solids* 23 (3), 411–421.